PHYSICAL REVIEW B **92**, 085423 (2015)

Van Hove singularity and ferromagnetic instability in phosphorene

A. Ziletti,[1] S. M. Huang,[2,3] D. F. Coker,[1] and H. Lin[2,3,*]
[1]Department of Chemistry, Boston University, 590 Commonwealth Avenue, Boston, Massachusetts 02215, USA
[2]Centre for Advanced 2D Materials and Graphene Research Centre, National University of Singapore, Singapore 117546
[3]Department of Physics, National University of Singapore, Singapore 117542

(Received 30 March 2015; revised manuscript received 25 June 2015; published 21 August 2015)

Using Wannier-function-based interpolation techniques, we present compelling numerical evidence for the presence of a saddle-point Van Hove singularity at the Γ point near the phosphorene Fermi energy. We show that in proximity of the Van Hove singularity the spin susceptibility presents the logarithmic temperature dependence typical of Liftshitz phase transitions. Furthermore, we demonstrate that the critical temperature for the ferromagnetic transition can be greatly increased (up to 0.05 K) if strain along the zigzag ridges is applied. Although the ferromagnetic state would be very difficult to experimentally reach, the logarithmic temperature behavior of the spin susceptibility due to the Van Hove singularity is found to persist at much higher temperatures (up to ~97 K).

DOI: 10.1103/PhysRevB.92.085423 PACS number(s): 73.20.At, 73.61.Cw, 73.20.−r

I. INTRODUCTION

Saddle-point Van Hove singularities [1] (VHSs) originate from saddle points in the band structure, around which the band curvature has opposite signs along two orthogonal directions. In two dimensions, the density of states (DOS) diverges at the VHS, and therefore arbitrary weak interactions can produce large effects in the electronic behavior, giving rise to instabilities in many aspects such as charge, spin, and/or pairing susceptibilities. Once the Fermi energy approaches a VHS, ferromagnetism [2,3], antiferromagnetism [4], and/or superconductivity [5–7] can be substantially enhanced.

The VHS is a topological critical point of the Fermi surface, across which the quantum Lifshitz phase transition takes place [8–11]. The Lifshitz transition for noninteracting systems is continuous and does not break symmetry. For interacting systems, however, the Lifshitz transition may become discontinuous and accompany symmetry breaking [9,12]. In cuprates, Hall coefficient measurements provide evidence for the Fermi surface topology change [13,14]. The Lifshitz transition is also proposed to change the Fermi liquid into the marginal Fermi liquid [15], and the VHS is thus argued to be responsible for the linear temperature (T) dependence of resistivity and the T-independent thermopower [16] observed in this regime [17–19]. Moreover, in the so-called "Van Hove scenario," the presence of a VHS near the Fermi energy is argued to play a major role in the high-T_c superconductivity of cuprates [20,21]. Given the strong influence of VHSs on the properties of materials, it is important to identify the presence and understand the role of these singularities, especially for technologically promising low-dimensional materials such as phosphorene.

Phosphorene [22,23], a single layer of black phosphorus, is the most recent addition to the growing family of two-dimensional (2D) materials. It is a semiconductor with high potential for applications in electronic and optoelectronic devices [24]. Despite the relative infancy of the field, few-layer phosphorene field effect transistors exhibit very high on-off current ratios [25,26] (exceeding 10^5) and ambipolar behavior [27], together with the highest hole mobility ever (4000 $\text{cm}^2/\text{V s}$) for a 2D material apart from graphene [28]. Phosphorene's pliable waved structure also allows for strain engineering of both effective masses and band gaps [29]. Strain can even induce a semiconductor to metal transition [23].

In this paper, we show that a VHS is present at the phosphorene Fermi energy, and we investigate the consequent ferromagnetic instability in both the unstrained and strained cases.

The paper is organized as follows: after introducing the computational methodology, in Sec. III A we present the electronic structure of phosphorene near the VHS, in Sec. III B we study the ferromagnetic instability (without strain), and finally in Sec. III C we investigate the effect of strain on the critical temperature T_c of the ferromagnetic transition.

II. COMPUTATIONAL DETAILS

The calculations involve the following three steps.

(i) A density functional theory (DFT) calculation is performed with a plane wave basis set, as implemented in the QUANTUM ESPRESSO package [30]. We use the PBEsol functional [31] for the exchange and correlation energy. A plane-wave basis set with a kinetic energy cutoff of 70 Ry (280 Ry) is used to represent the electronic wave function (charge density). The core electrons are described via the projected-augmented wave (PAW) [32] method; 12.9 Å of vacuum are added in the direction normal to the monolayer to avoid spurious interactions between periodic replicas. Both lattice parameters and atomic positions are relaxed until the forces on each atom are less than 10^{-3} eV/Å and the pressure is less than 1 kbar. After lattice relaxation, the phosphorene crystal parameters are $a_x = 3.28$ Å and $a_y = 4.44$ Å, in agreement with a previous study [23]. The optimized configuration of the phosphorene monolayer is presented in Fig. 1(a). In this DFT calculation, the Brillouin Zone (BZ) is sampled using a Γ-centered $60 \times 48 \times 1$ Monkhorst-Pack (MP) grid [33]. This calculation will serve as a benchmark for the Wannier interpolation of the band structure [Figs. 1(b) and 1(c)].

---

[*] nilnish@gmail.com

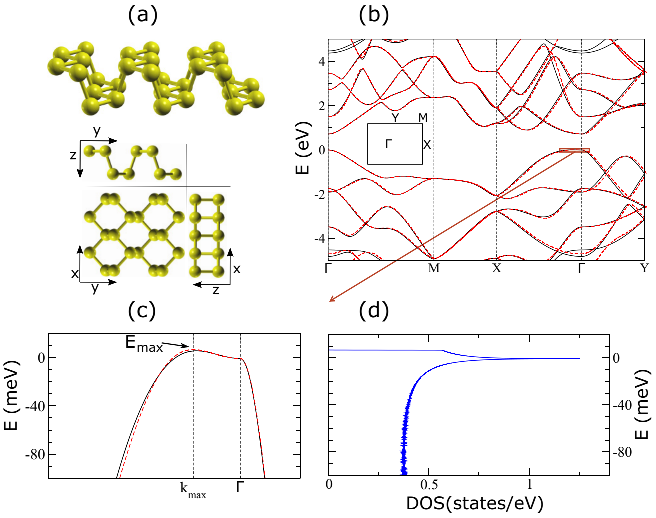

FIG. 1. (Color online) (a) Crystal structure of phosphorene and its projections on the y-z, x-y, and x-z planes. (b) DFT-PBEsol electronic band structure (solid black line) and its Wannier interpolation (dashed red line). The Brillouin zone is also shown. (c) Detail of the electronic band structure and (d) DOS in a small region near the VHS. The energy at the VHS is set to zero.

(ii) Using the self-consistent charge density obtained from step (i), we evaluate the required input quantities for the Wannier calculation (energy eigenvalues, overlap matrices, and projections [34]) on a relatively coarse 10 × 8 × 1 mesh for the unstrained case (Secs. III A and III B), and a 30 × 8 × 1 mesh for the strained case (Sec. III C). These k-point meshes are fine enough to provide converged Wannier functions. The calculations are performed with QUANTUM ESPRESSO and its postprocessing subroutine PW2WANNIER90.

The aim of the two previous steps is to obtain the maximally localized Wannier functions [34,35] (MLWFs) to be later used for the very dense k-point sampling around the VHS.

(iii) With the energy eigenvalues, overlap matrices, and projections obtained from step (ii), we construct the MLWFs according to the procedure presented in Refs. [34,36]. The resulting Wannier functions consist of three p orbitals centered on each P atom, leading to the Wannierization of six valence and six conduction bands (there are four P atoms in the phosphorene unit cell).

One of the main advantages of the maximally localized Wannier representation of the DFT orbitals is that quantities calculated on a coarse reciprocal-space grid can be used to interpolate on a much finer grid with low computational cost. The Wannier interpolation is particularly useful when a fine BZ sampling is required to converge the quantity of interest. In this work, such quantities are the DOS and the valence band in a small region around the VHS. For the DOS calculation, an extremely dense Wannier interpolated mesh of $(4 \times 10^4) \times (3.2 \times 10^4) \times 1$—corresponding to ~1.3 billion k points in the BZ—is used to capture the sharp peak in the DOS due to the VHS. We use a smearing of 7×10^{-4} eV. Similarly, a Wannier interpolation with a reciprocal lattice spacing of $\Delta k_{x,y} = (2 \times 10^{-3}) \times 2\pi/a_{x,y}$ corresponding to a 500 × 500 × 1 MP grid is employed for the contour plot of the valence band around the VHS. All MLWF calculations are performed with the WANNIER90 package [37].

To further validate the PBEsol results, we have performed additional calculations with the local LDA functional [38], the semilocal Perdew-Burke-Ernzerhof (PBE) functional [39], the screened-hybrid HSE06 functional [40], and the GW method [41,42] in order to elucidate the position of the valence band maximum. In particular, the HSE06 functional and the GW method are known to provide a more accurate description of the electronic properties of semiconductors and insulators than local or semilocal density functionals [43,44].

In local density approximation (LDA) and PBE calculations, atomic positions and lattice parameters are relaxed until the forces are less than 10^{-3} eV/Å and the pressure less than 1 kbar. The BZ is sampled with a Γ-centered 60 × 48 × 1 MP grid as in the case of PBEsol calculations. The HSE06 corrections are instead calculated self-consistently using the PBE relaxed lattice parameters and atomic positions, together with a 12 × 12 × 1 MP grid. The band structure is then obtained using the derived Wannier functions in a similar fashion to the PBEsol calculations outlined above.

The GW calculations are performed in two steps. First, atomic positions and relaxed lattice geometries are calculated with the PBE functional and norm-conserving Troullier-Martins pseudopotentials [45]. Then the GW corrections are computed following the method proposed by Hybertsen and Louie [41]. We include 138 bands in the evaluation of the dielectric matrix and the self-energy, with a cutoff of 4 Ry for the dielectric matrix; convergence was checked including up to 384 bands. A supercell of 20 Å in the direction perpendicular to the monolayer and a slab-truncation potential [46] are used in these GW calculations to avoid spurious interactions with periodic replicas of the system. A fine MP grid is employed in the direction of the VHS (100 × 8 × 1) to distinguish the top of the valence band from the Γ point, thus providing evidence for the presence of the VHS. All GW calculations are performed with the plane-wave based ABINIT package [47].

III. RESULTS AND DISCUSSION

A. Electronic band structure and Van Hove singularity

Phosphorene is a semiconductor with a relatively large band gap that is underestimated (0.72 eV) at the PBEsol level (a well-known deficiency of local and semilocal DFT functionals [48]), and enlarged at 1.6–2.0 eV when GW corrections [41,42] are included [49–51]. The electronic band structure of phosphorene, calculated with the PBEsol functional, is shown in Fig. 1(b). The black solid line represents a standard plane-wave DFT calculation, while the red dotted line is the band structure obtained through a Wannier interpolation. Our Wannier interpolation is very accurate, over a broad range of energies. In particular, at Γ point, the DFT band structure and the Wannier interpolation differ by less than 10^{-5} eV.

In agreement with recent studies [23,51,52], we find that the top of the valence band is slightly away from the Γ point for the LDA, PBE, and PBEsol functionals. Using these three DFT functionals, we consistently find that the top of the valence band is displaced from Γ along the Γ-X direction, which is the direction along the phosphorene zigzag ridges

TABLE I. Position of the valence band maximum, $k_{\max}$, and its energy, $E_{\max}$, relative to the Γ point [see Fig. 1(c)] calculated with different computational methods and various strains, x_{str}, along the x direction of the phosphorene lattice. When $k_{\max} = 0$ (and thus $E_{\max} = 0$) the top of the valence band coincides with the Γ point, and therefore the VHS is not present.

	LDA		PBE		PBEsol		HSE06		*GW*	
	$k_{\max}$ (A^{-1})	$E_{\max}$ (meV)	$k_{\max}$ (A^{-1})	$E_{\max}$ (meV)	$k_{\max}$ (A^{-1})	$E_{\max}$ (meV)	$k_{\max}$ (A^{-1})	$E_{\max}$ (meV)	$k_{\max}$ (A^{-1})	$E_{\max}$ (meV)
$x_{\text{str}} = -8\%$	0.256	79.4	0.275	62.3	0.260	73.3	0.271	54.4	0.269	53.8
$x_{\text{str}} = -6\%$	0.212	51.9	0.213	32.9	0.211	44.9	0.168	28.9	0.206	25.5
$x_{\text{str}} = -4\%$	0.175	33.1	0.161	15.1	0.175	27.8	0.129	13.0	0.147	8.9
$x_{\text{str}} = -2\%$	0.145	20.2	0.113	5.1	0.136	14.0	0.092	3.6	0.083	1.1
$x_{\text{str}} = 0\%$	0.119	11.6	0.063	0.7	0.105	6.6	0.029	0.05	0.000	0.0
$x_{\text{str}} = +4\%$	0.067	1.9	0.000	0.0	0.033	0.1	0.000	0.0	0.000	0.0

[see Fig. 1(a)]. The detailed symmetry analysis presented in Ref. [52] attributes the absence of direct band gap to the counteracting effects (in the $\mathbf{k}\cdot\hat{\mathbf{p}}$ approximation [53]) of states of different symmetries on the valence band around the zone center.

To further validate these results, we have carried out calculations using the screened hybrid HSE06 functional and the *GW* approximation, which are known to improve the description provided by local or semilocal DFT functionals (such as LDA, PBE, and PBEsol), not only regarding band gaps, but also concerning the band dispersion in semiconductors and insulators [43,44,54–58].

To quantitatively characterize the valence band maximum, we define $\mathbf{k}_{\max} \equiv (k_{\max},0)$ as the wave vector at which the valence band has a maximum, and $E_{\max}$ as the difference in energy between the valence band maximum and the value of the valence band at the Γ point. The results obtained with various computational methods and different strains are reported in Table I. As mentioned before, in absence of strain, LDA, PBE, and PBEsol gives a valence band top slightly away from the Γ point, with $E_{\max}$ ranging approximately from 1 to 12 meV. With the HSE06 functional, the valence band top is slightly displaced from Γ; however, the calculated value of $E_{\max}$ is so small (0.05 meV) that it can be considered zero. Also the *GW* method—in the absence of strain—predicts phosphorene to be a direct band-gap semiconductor.

We then apply strain along the x direction, changing the lattice parameter a_x to be $a_x(1+x_{\text{str}})$, where a positive (negative) value of x_{str} indicates tensile (compressive) strain. The results are shown in Table I. Application of compressive strain moves the valence band top away from the Γ point in all computational methods. In particular, with the HSE06 functional and the *GW* method, the top of the valence band is displaced from the Γ point with a 2% strain; larger strains monotonically increase both $k_{\max}$ and $E_{\max}$ with $E_{\max} \sim 54$ meV for a strain of 8% according to the *GW* method. In contrast, tensile strain moves the top of the valence band towards the Γ point, and eventually removes the VHS singularity.

Having established that a VHS near the phosphorene Fermi energy is either present or can be strain induced using a wide range of electronic structure descriptions, hereafter we consider as an explanatory example the case of the PBEsol functional. Other functionals and the *GW* method are expected to yield similar general results.

A magnification of the valence band maximum is shown in Fig. 1(c). From Fig. 1(c), we notice that the valence band has a saddle point at Γ. In the reciprocal-space neighborhood of this point, the principal curvature is electronlike along the Γ-X path [from the left in Fig. 1(c)], while it is holelike in the Γ-Y path [from the right in Fig. 1(c)]. Thus, at the Γ point there is a crossover from electronlike to holelike conduction that originates at the VHS. The DOS, calculated on an ultrafine grid of ~1.3 billion k points, is shown in Fig. 1(d). It exhibits a divergent behavior at the energy position of the VHS, as expected for a 2D lattice. In contrast to the saddle-point behavior at Γ, the valence band has a maximum at $\mathbf{k}_{\max}$ and therefore the DOS shows a steplike drop to zero at this point [59].

Three-dimensional (3D) and 2D plots of the phosphorene valence band in the neighborhood of the VHS (Γ point) are depicted in Figs. 2(a) and 2(b), respectively. The electronlike dispersion along the Γ-X path [cut-x in Fig. 2(a)] and the holelike dispersion in the Γ-Y path [Cut-y in Fig. 2(a)] are evident. The VHS has indeed the topology of a 3D saddle point. Moreover, the valence band is anisotropic at the Γ point, with strong dispersion along Γ-Y [armchair direction; see Fig. 1(a)], while it is nearly flat on Γ-X [zigzag direction; see Fig. 1(a)]. The large difference in magnitude of the effective masses along the two directions gives to the VHS an extended structure, as shown in Fig. 2(b). From a fitting of the local curvature of the valence band around the Γ point, we obtain $m_x/m_y \sim 27$, where m_x and m_y are the effective masses on the Γ-X and Γ-Y path, respectively.

In the limit of infinite mass in one direction (i.e., flat band in one direction, vanishing curvature) the saddle point becomes extended, giving rise to a so-called extended VHS (EVHS). EVHSs have been experimentally observed in doped graphene [60] and in some layered cuprate superconductors [61–63]. In 2D materials, the DOS is known to diverge logarithmically at the VHS, while in an EVHS the energy dispersion is quasi-one-dimensional, and the DOS has a much stronger square-root divergence [59]. Therefore, due to the anisotropy of the phosphorene band structure, the VHS has an extended character that might amplify its effects on the material properties.

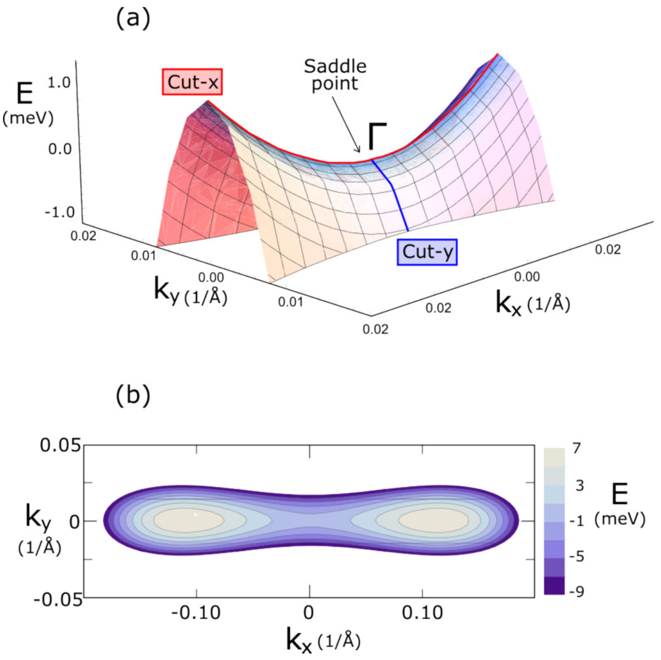

FIG. 2. (Color online) (a) 3D plot of the phosphorene valence band around the VHS (Γ point) (PBEsol functional). Cut-$x(y)$ indicates the Γ-$X(Y)$ path used in the band structure calculation. (b) 2D contour plot of the valence band in a larger region around Γ. The contour lines are drawn at 2 meV intervals. The energy at the VHS is set to zero in both plots.

B. Ferromagnetic instability

As mentioned in the Introduction, the presence of a VHS at the Fermi energy can create ferromagnetic, antiferromagnetic, or superconducting instabilities. In contrast to cuprates where the VHS points are at $(\pi,0)$ and $(0,\pi)$, in phosphorene the VHS point is at Γ and therefore we can exclude antiferromagnetism since no inter-VHS scattering can induce this instability. Furthermore, for highly anisotropic masses (see Sec. III A), $m_x/m_y \gg 1$, similar to the $t-t'$ Hubbard model with large t'/t (>0.276), the ferromagnetic instability will win over other instabilities [4,7,64]. As a result, we can omit also superconductivity and consider only ferromagnetism.

The extremely fine structure of the VHS in phosphorene requires a very high resolution calculation of the band structure. To make the calculation accessible, instead of using the band structure from the Wannier interpolation, we approximate it here by an analytic single-band model. Consistent with Fig. 1(c) and Fig. 2, the low-energy physics in the neighborhood of the VHS can be described by

$$E(k_x,k_y) = \tfrac{1}{2}\alpha k_x^2 - \tfrac{1}{4}\beta k_x^4 - \tfrac{1}{2}\alpha' k_y^2, \tag{1}$$

which characterizes the saddle point at Γ (opposite signed band masses along k_x and k_y) and band inflection along k_x. As in the previous section, the VHS energy at Γ, E_{VHS}, is set to zero while the band maximum at $k_{\max}$ is $E_{\max}$. To fit the DFT-PBEsol calculations, the band parameters follow the relations: $\alpha'/\alpha = m_x/m_y = 27.02$, $\sqrt{\alpha/\beta} = |k_{\max}| = 0.104\,\text{Å}^{-1}$, and $\alpha^2/4\beta = E_{\max} = 6.6$ meV.

This simple model captures the energy dispersion behavior near the VHS and, since the parameters of the model are determined directly from the DFT calculation, it allows us to investigate the magnetic instability quantitatively.

Obviously, a ferromagnetic instability can take place only in metallic or semimetallic systems, and therefore some amount of doping is required for phosphorene to exhibit metallic behavior. To study the effects arising from the presence of the VHS, hereafter we thus assume the Fermi energy to be exactly at the VHS, $E_{\mathrm{VHS}} = 0$, unless otherwise stated. In the case of the PBEsol functional, the amount of (hole) doping necessary to reach the VHS (from the top of the valence band $E_{\max}$) is found to be approximately 4.2×10^{-3} electrons per unit cell, corresponding to a surface doping concentration of 1.4×10^{12} cm^{-2} for each spin.

Given the energy dispersion in Eq. (1), it is possible to derive an exact analytical expression for the DOS, $N(E)$ (see Appendix A for a complete derivation):

$$N(E) = \begin{cases} -\sqrt{\frac{2}{\beta\alpha'}}\,\frac{a_x a_y}{\pi^2 k_+} K\left(\sqrt{1-p^{-2}}\right) & \text{if} \quad E \geqslant 0 \\ -\sqrt{\frac{2}{\beta\alpha'}}\,\frac{a_x a_y}{\pi^2 |k_-|}\,\frac{1}{\sqrt{|p|^2+1}} K\left(\sqrt{\frac{1}{1+|p|^{-2}}}\right) & \text{if} \quad E < 0, \end{cases} \tag{2}$$

where we have defined

$$k_\pm = k_{\max}\sqrt{1 \pm \sqrt{1 - E/E_{\max}}}, \qquad p^2 = \frac{k_+^2}{k_-^2} \tag{3}$$

and $K(k)$ is the complete elliptic integral of the first kind. The quantities a_x and a_y are the phosphorene lattice parameters, as defined in Sec. II.

Since we are mainly interested in the behavior of the DOS at the VHS, we take the limit $E \to 0$ in Eq. (2) to obtain (see Appendix A)

$$N(E \to 0_\pm) = \frac{a_x a_y}{2\pi^2\sqrt{\alpha\alpha'}}[\ln(E_{\max}/E) + O(1)]. \tag{4}$$

The model of Eq. (1) therefore exhibits a logarithmically divergent DOS and it is proportional to the geometric mean mass, $\sqrt{m_x m_y} \propto 1/\sqrt{\alpha\alpha'}$, so in the limit of small energies we can approximate the DOS as

$$N(E) \approx N_0 \ln(\Lambda/E), \tag{5}$$

where $N_0 = \frac{a_x a_y}{2\pi^2\sqrt{\alpha\alpha'}} = 0.0588\,\mathrm{eV}^{-1}$, and Λ is an energy cutoff of the order of $E_{\max}$. In this approximation, the DOS only includes contributions from states around Γ. This is fully justified since the behavior of the DOS near the VHS is obviously governed by its divergence at $E = 0$ (Γ point), and therefore finite (not diverging) contributions from other regions in the Brillouin zone can be neglected.

With the logarithmic DOS one can derive (see Appendix B) an expression for the bare spin susceptibility that shows a dependence on the logarithm of the inverse temperature,

$$\chi(T) = -\int_{\mathrm{BZ}} \frac{d^2k}{(2\pi)^2}\frac{\partial n_{\mathrm{F}}(E_k)}{\partial E_k} \tag{6}$$

$$\approx N_0 \ln(\omega_D/T), \tag{7}$$

where n_{F} is the Fermi distribution, E_k are the energy (Kohn-Sham) eigenvalues, and ω_D is a fitting constant of the order of $E_{\max}$. We also set the Boltzmann constant k_{B} to unity. The logarithmic divergence at low temperatures [Eq. (7)] is

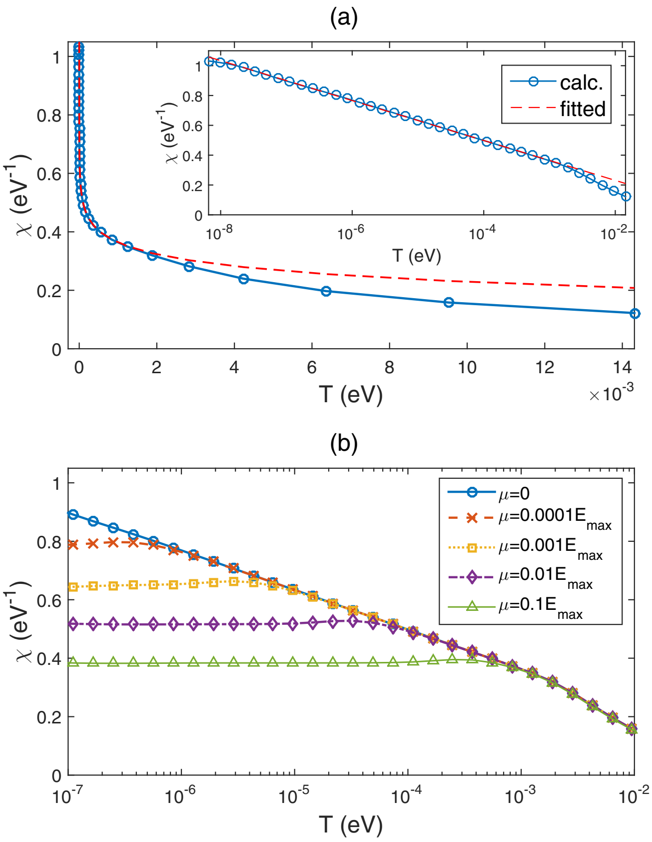

FIG. 3. (Color online) (a) Temperature dependence of the bare spin susceptibility χ calculated directly from Eq. (6) (blue dots) or approximated with the logarithmic divergence in Eq. (7) (dashed red line). The low-temperature behavior for $T < T^* \sim 1.5$ meV is seen in the inset to follow the logarithmic law. The dashed red line is fitted to Eq. (7) with $\omega_D = 0.5004$ eV. The Fermi level is set to $E_{\mathrm{VHS}} = 0$. (b) Spin susceptibilities χ at different Fermi energies μ. Away from the VHS, the low-temperature logarithmic behavior stops at $T \approx \mu$ and turns into Pauli susceptibility.

confirmed by explicit calculation of the spin susceptibility using Eq. (6), as shown in Fig. 3(a).

Notably, the logarithmic behavior is present only when the temperature is lower than T^*, which is defined as the temperature above which the spin susceptibility starts deviating from the logarithmic behavior. Thus, above $T^* \sim$ 17 K (corresponding to an energy scale of 1.5 meV), we observe deviation of the susceptibility from the logarithmic law as seen in the inset of Fig. 3(a). This temperature T^* is related to the energy scale $E_{\max}$. We have checked this apparent relationship between T^* and $E_{\max}$ by comparing susceptibilities for different band parameters β (and thus $E_{\max}$) in Eq. (1), and we indeed see proportionality between T^* and $E_{\max}$ (not shown). It is also found that the susceptibility increases with $E_{\max}$ as expected from the energy cutoff and fitting constant dependence in Eqs. (5) and (7), respectively.

Next, we examine the effect of doping on the ferromagnetic instability, considering various chemical potential shifts μ. The susceptibility was calculated numerically and the results are presented in Fig. 3(b), in which the Fermi energy is shifted to μ above E_{VHS} (the energy of the VHS, or Γ). Figure 3(b) shows that even away from the VHS point, the logarithmic-T behavior of the susceptibility is still preserved for $T < T^*$. However, for each value of μ, we see that the logarithmic increase of χ with decreasing T stops at μ, below which the susceptibility becomes constant suggesting a transition to Pauli paramagnetism at low temperatures. This different behavior for large and small T (with respect to μ) can thus be understood directly from the expression of the bare spin susceptibility as outlined in Appendix B.

It is in fact possible to obtain analytical estimates for χ in both regimes (please refer to Appendix B for a complete derivation). For $T \gg \mu$, the susceptibility has the form

$$\chi(T \gg \mu) \approx N_0 \ln(\omega_D/T) \cosh^{-2}(\mu/2T). \tag{8}$$

We observe the logarithmic-T behavior, typical of Liftshitz phase transitions. Moreover, for $\mu/T \to 0$, $\cosh^{-2}(\mu/2T) \to 1$ and therefore, in this limit, χ for the doped system has precisely the same behavior as in the undoped case, as confirmed by the numerical results presented in Fig. 3(b). In contrast, for $T \ll \mu$ the susceptibility is found to be independent of T:

$$\chi(T \ll \mu) \approx N_0 \ln(\bar{\Lambda}/\mu), \tag{9}$$

where $\bar{\Lambda}$ is an energy cutoff $\bar{\Lambda} < E_{\max}$. This saturation of χ agrees well with the numerical results presented in Fig. 3(b), and it originates from the infrared cutoff of the excitations due to the shifted thermal distribution (see Appendix B).

Now we estimate the ferromagnetic transition temperature. Let us assume a Hubbard interaction of strength U between intraorbital spins. According to the Stoner criterion [65], the magnetic transition occurs when $U_\nu \chi(T) = 1$. Here U_ν, which is defined by U times the average weight W_ν at the Fermi energy for a particular orbital ν, is regarded as the effective interaction of orbital ν.

According to the BCS theory [66], for a metal, the superconductivity arises as a result of introducing an infinitesimal (attractive) interaction between the electrons at zero temperature. Analogously, in our system, as the density of states diverges, we expect that infinitesimal interactions can drive the ferromagnetic transition at zero temperature. From the Stoner criterion, the critical temperature thus follows the BCS form,

$$T_c = \omega_D \exp(-1/N_0 U_\nu), \tag{10}$$

where the geometric mean mass, appearing in N_0 [as indicated below Eq. (5)], determines the DOS at the Fermi energy. Equation (10) is also consistent with the renormalization group result for the spin susceptibility, which exhibits the same logarithmic temperature behavior [64,67]. Here, the quantity ω_D is a suitable energy bound for the model. In general, it could be, for example, the interaction strength or the bandwidth (the scale of the VHS logarithmic tail). In our case, since the VHS is close to the valence band maximum, $E_{\max}$ (above which a large gap from the conduction band is present), the VHS logarithmic tail ends at $E_{\max}$, and therefore $\omega_D \approx E_{\max}$. Using the BCS formula in Eq. (10), one can obtain the magnetization directly.

The effective interaction V_{eff} can be evaluated using the Kohn-Sham orbitals from the DFT calculation. Let us define orbital operators ψ_m and band operators ϕ_ν. The relation between them is a unitary transformation $\psi_m(\mathbf{k}) = \sum_\nu A_{m,\nu}(\mathbf{k})\phi_\nu(\mathbf{k})$ where $A(\mathbf{k})$ is the unitary matrix that diagonalizes the Bloch Hamiltonian. The Hubbard on-site (intraorbital) interaction is

$$H_U = U \sum_{\mathbf{R},m} \psi^\dagger_{m\uparrow}(\mathbf{R})\psi_{m\uparrow}(\mathbf{R})\psi^\dagger_{m\downarrow}(\mathbf{R})\psi_{m\downarrow}(\mathbf{R}), \tag{11}$$

where $\mathbf{R}$ is the real space lattice vector and $\psi_{m\uparrow,\downarrow}$ are the Kohn-Sham spin orbitals.

Since only the valence band (VB) is included in our low-energy model [Eq. (1)], we include only the intraband scattering terms from the Hubbard model. Moreover, at $T = 0$, only states from the Fermi surface contribute to the susceptibility. After these considerations, the effective interaction V_{eff} for $\nu = \text{VB}$ is

$$V_{\text{eff}} \approx U_\nu \sum_{\mathbf{k}_1,\mathbf{k}_2,\mathbf{k}_3} \phi^\dagger_{\nu\uparrow}(\mathbf{k}_1)\phi_{\nu\uparrow}(\mathbf{k}_2)\phi^\dagger_{\nu\downarrow}(\mathbf{k}_3)\phi_{\nu\downarrow}(\mathbf{k}_1 + \mathbf{k}_3 - \mathbf{k}_2), \tag{12}$$

where the momenta $\mathbf{k}_1$, $\mathbf{k}_2$ and $\mathbf{k}_3$ are in the neighborhood of the Fermi surface and the interaction strength

$$U_\nu = U W_\nu = U \left\langle \sum_m |A_{m,\nu}(\mathbf{k})|^4 \right\rangle_{\text{FS}} \tag{13}$$

is averaged on the Fermi surface in the sense that the momentum dependence can be neglected since the Fermi surface around the VHS is small.

From the DFT results, we obtain an average weight, W_ν, for the contributing orbitals of about 0.2. This orbital weight significantly reduces the critical temperature. For example, using the criterion $U_\nu \chi(T_c) = 0.8$ and at $U = 4$ eV, the critical temperature T_c for ferromagnetism is only about 4 μK.

Doping can destroy ferromagnetism even at zero temperature when $N_0 U_\nu \ln(\omega_D/\mu) < 1$. Although interorbital interactions might slightly enhance T_c, the Stoner criterion applied to the bare susceptibility typically overestimates the critical temperature since particle-particle correlations would give large corrections to the self-energy [67–69]. As a result, this ferromagnetic state would be difficult to reach.

C. Effect of strain on the Van Hove singularity and on the critical temperature

Strain can have a large effect on phosphorene's pliable waved structure, and therefore it represents a natural way to tune the band parameters of the VHS, in order to increase T_c. In particular, from Eq. (10) we notice that, for a fixed effective interaction, the critical temperature can be varied in two ways. One way is to increase ω_D (or equivalently E_{max}; see Sec. III B), which will cause a linear increase in T_c. The second and more prominent way is to increase N_0, which will result in an exponential increase in T_c. This can be accomplished, for instance, by reducing the dispersion in both x and y directions near the Γ point [see Eqs. (1) and (5)].

We find that strain along the armchair direction [y axis in Fig. 1(a)] does not significantly alter the critical temperature, with a modest ninefold increase in T_c (~36 μK) for a tensile strain of 3%.

TABLE II. Parameters related to the VHS for different strains on the zigzag direction [x axis in Fig. 1(a)]. For $T < T^*$, the susceptibility follows the logarithmic temperature dependence of Eq. (7). The PBEsol functional is used.

	$x_{\text{str}} = -4\%$	$x_{\text{str}} = 0\%$	$x_{\text{str}} = +4\%$
$\mathbf{k}_{\text{max}}$ (1/Å)	(0.175,0)	(0.105,0)	(0.033,0)
E_{max} (meV)	27.8	6.6	0.1
N_0 (eV^{-1})	0.0374	0.0588	0.1909
T^* (K)	97	17	0.23
T_c (K)	5×10^{-7}	4×10^{-6}	5×10^{-2}

The situation, however, is significantly different for strain along the zigzag ridge direction [x axis in Fig. 1(a)]. The most relevant quantities for representative x-strain values are listed on Table II.

Compressive x strain of 4% slightly reduces N_0 (see Table II), and leads to a decrease in T_c to only 0.5 μK. In contrast to this N_0, we see from Table II that E_{max} increases with this compressive x strain. Due to the proportionality between E_{max} and T^*, the spin susceptibility starts to follow the logarithmic-T behavior—the signature of the VHS—at higher temperatures than the unstrained case. For example, we see that a compressive x strain of 4% leads to T^* of about 97 K (8.4 meV) [see Fig. 4(a), yellow squares]. Due to the relatively high temperatures involved, the logarithmic-T behavior in the spin susceptibility could in principle be observable experimentally, thus providing compelling evidence for the presence of the VHS.

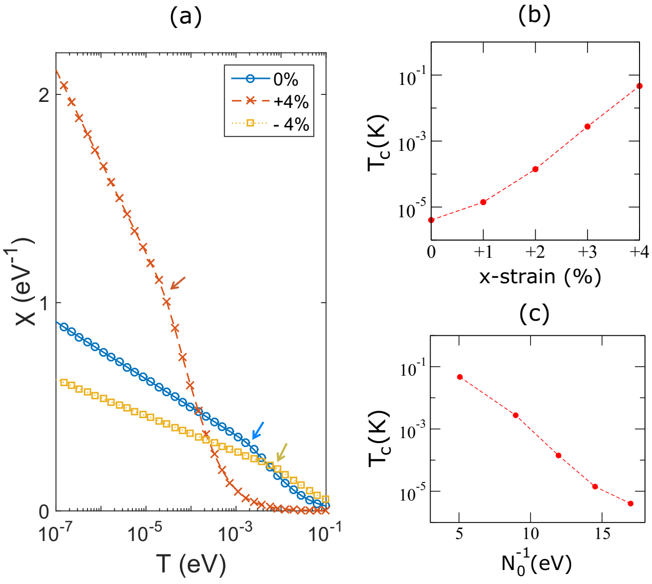

FIG. 4. (Color online) Effect of zigzag ridge [x axis in Fig. 1(a)] strain on the VHS. (a) Temperature dependence of the bare spin susceptibility χ for different strains. The arrows indicate the temperature T^* at which the susceptibility starts to deviate from the logarithmic behavior. (b) Critical temperature T_c as a function of strain. (c) T_c versus N_0^{-1}. The behavior of T_c still follows the exponential law of Eq. (10) even if strain is applied.

In contrast, tensile x strain has the opposite effect on the band parameters: while $E_{\max}$ diminishes, N_0 is greatly enhanced. Notably, the critical temperature exhibits an exponential dependence on tensile strain, as depicted in Fig. 4(b). For a 4% strain, the critical temperature is about 0.05 K. Even though this corresponds to a 10^4-fold increase in T_c with respect to the unstrained case, this magnetic state will hardly be seen experimentally due to the very low temperatures required. We also observe that the logarithmic divergence becomes the dominant contribution at around $T^* \sim 0.23$ K (0.002 meV) [Fig. 4(a), orange crosses], a much lower value compared to the unstrained case resulting from the flattening of the valence band (and consequently diminished $E_{\max}$), caused by the applied stress.

The physics behind the strain dependence of the VHS is simple. The act of stretching will decrease the hoppings between phosphorus atomic orbitals, thus reducing the bandwidth. As the dispersion decreases, we expect that α and α' in Eq. (1) become smaller and hence the density of states N_0 increases. The act of compressing will show the opposite trend. Because the band inflection is along k_x, x strain has a larger effect on α compared to y strain, explaining our findings.

Finally, we observe that the critical temperature still follows the exponential law of Eq. (10), even when strain is applied, as shown in Fig. 4(c). For higher stress, T_c could deviate from Eq. (10), since $E_{\max}$ diminishes ($\sim 10^{-4}$ eV for a 4% tensile strain) and therefore narrows the VHS divergence, limiting the increase of the critical temperature.

IV. CONCLUSIONS

We have used Wannier-function-based interpolation techniques to investigate the VHS at the Γ point near the phosphorene Fermi energy with more than a billion k points. Thanks to this extreme resolution, we are able to present compelling numerical evidence for the presence of a VHS near the phosphorene Fermi energy. As a result of its close proximity to the valence band maximum, the VHS can be reached with a hole doping concentration on the order of 10^{12} cm^{-2}, easily achievable by chemical doping or ionic-liquid gating [70].

Furthermore, we have calculated an exact expression for the DOS near the VHS, and we have demonstrated that the spin susceptibility presents a logarithmic-T behavior, signature of the VHS, and consequent Lifshitz phase transition.

We have also shown that the critical temperature can be increased up to 0.05 K by applying a modest strain to the phosphorene pliable waved structure. Although this ferromagnetic state would be very difficult to reach experimentally, the logarithmic temperature behavior of the spin susceptibility due to the presence of the VHS could be observed because it persists at higher temperatures ($T^* \sim 17$ K for the unstrained case, and $T^* \sim 97$ K for a 4% tensile strain along the zigzag ridges).

There are numerous experimental techniques able to detect the presence of VHSs. For example, the scanning tunneling microscope (STM) measures the tunneling differential conductance, which is proportional to the local DOS [71], and therefore represents an ideal tool to detect VHSs. This technique has been used to observe VHSs in other 2D materials such as twisted multilayer graphene [72], or the cuprate superconductor Bi-2201 [63]. Furthermore, angle-resolved photoemission spectroscopy (ARPES) can detect saddle points in the single-particle energy dispersion, as employed for numerous cuprate compounds [61,62,73,74] and doped graphene [60]. Finally, the Knight shift [75] in nuclear magnetic resonance experiments could provide evidence for the change in spin susceptibility in proximity of the VHS.

ACKNOWLEDGMENTS

We thank Chuang-Han Hsu for technical assistance. A.Z. and D.F.C. acknowledge NSF Grant No. CHE-1301157 and also an allocation of computational resources from Boston University's Office of Information Technology and Scientific Computing and Visualization. H.L. acknowledges the Singapore National Research Foundation for the support under NRF Award No. NRF-NRFF2013-03. A.Z. and S.M.H. contributed equally to this work.

APPENDIX A: EXACT DERIVATION OF THE DENSITY OF STATES

In this Appendix, we present an analytical derivation of the DOS for phosphorene around the VHS. According to Eq. (1), the dispersion relation of the valence band around the Γ point has the form

$$E_k = \tfrac{1}{2}\alpha k_x^2 - \tfrac{1}{4}\beta k_x^4 - \tfrac{1}{2}\alpha' k_y^2 \tag{A1}$$

with $\alpha,\beta,\alpha' > 0$. The valence band has its energy extreme at $E_{\max} = \alpha^2/4\beta$ when $(k_x,k_y) = (k_{\max},0)$ and $k_{\max} = \sqrt{\alpha/\beta}$. Moreover, there is a VHS at energy $E_{\mathrm{VHS}} = 0$ originating from states near $k_x = 0$.

By definition, the DOS per spin per unit area is

$$\begin{aligned} N(E) &= \int \frac{dk_x dk_y}{(2\pi)^2}\delta(E - E_k) \\ &= \frac{2}{(2\pi)^2}\int dk_x \int_{k_y \geqslant 0} dk_y \frac{1}{\left|\partial_{k_y} E_k\right|}\delta\left(k_y - k_y^E\right) \\ &= \frac{1}{\sqrt{2\alpha'}\pi^2}\int_{k_x \geqslant 0} dk_x \frac{1}{\sqrt{\frac{\alpha}{2}k_x^2 - \frac{\beta}{4}k_x^4 - E}}, \end{aligned} \tag{A2}$$

where k_y^E satisfies $E = \frac{1}{2}\alpha k_x^2 - \frac{1}{4}\beta k_x^4 - \frac{1}{2}\alpha'(k_y^E)^2$.

The integration range is limited by the fact that the square-root term has to be real. After some algebra, one can show that the integral range is $k \in [\max(0,k_-),k_+]$ with

$$k_\pm = \sqrt{\frac{\alpha}{\beta} \pm \sqrt{\left(\frac{\alpha}{\beta}\right)^2 - \frac{4E}{\beta}}} = k_{\max}\sqrt{1 \pm \sqrt{1 - E/E_{\max}}}. \tag{A3}$$

Thus, if $E < 0$, k_- is not purely real, and the lower bound is zero. Therefore, we have

$$\begin{aligned} &\int_0^{k_+} dk_x \frac{1}{\sqrt{\frac{\alpha}{2}k_x^2 - \frac{\beta}{4}k_x^4 - E}} \\ &\quad = \int_0^{k_+} dk_x \frac{1}{\sqrt{\left(-\frac{\beta}{4}\right)\left(k_x^2 - k_+^2\right)\left(k_x^2 - k_-^2\right)}} \end{aligned}$$

$$= \frac{-2i}{\sqrt{\beta}k_-}\int_0^1 dx\,\frac{1}{\sqrt{(1-x^2)(1-p^2x^2)}}$$
$$= \frac{-2i}{\sqrt{\beta}k_-}F\left(\frac{\pi}{2},p\right) = \frac{-2i}{\sqrt{\beta}k_-}K(p), \tag{A4}$$

where we have defined

$$p^2 \equiv \frac{k_+^2}{k_-^2} = \frac{E_{\max}}{E}\left(1+\sqrt{1-\frac{E}{E_{\max}}}\right)^2 \tag{A5}$$

and introduced $F(\phi,k)$ the incomplete elliptic integral of the first kind and $K(k)$ the complete elliptic integral of the first kind. They are related here by $F(\frac{\pi}{2},k) = K(k)$.

On the other hand, if $E > 0$ ($k_- > 0$), the lower bound is k_- and we will deal with

$$\int_{k_-}^{k_+} dk_x\,\frac{1}{\sqrt{\frac{\alpha}{2}k_x^2 - \frac{\beta}{4}k_x^4 - E}}$$
$$= \int_{k_-}^{k_+} dk_x\,\frac{1}{\sqrt{\left(-\frac{\beta}{4}\right)\left(k_x^2-k_+^2\right)\left(k_x^2-k_-^2\right)}}$$
$$= \frac{-2i}{\sqrt{\beta}k_-}\int_{p^{-1}}^1 dx\,\frac{1}{\sqrt{(1-x^2)(1-p^2x^2)}}$$
$$= \frac{-2i}{\sqrt{\beta}k_-}\left(\frac{-i}{p}\right)F\left(\frac{\pi}{2},\sqrt{1-p^{-2}}\right)$$
$$= \frac{-2}{\sqrt{\beta}k_+}K(\sqrt{1-p^{-2}}). \tag{A6}$$

In Eqs. (A4) and (A6), we have used the integral formulas:

$$\int_0^u dx\,\frac{1}{\sqrt{(1-x^2)(1-p^2x^2)}}$$
$$= \frac{1}{2}\int_0^{u^2} dz\,\frac{1}{\sqrt{z(1-z)(1-p^2z)}} = F(\arcsin(u),p), \tag{A7}$$
$$\int_u^1 dx\,\frac{1}{\sqrt{(1-x^2)(1-p^2x^2)}}$$
$$= \frac{1}{2}\int_{u^2}^1 dz\,\frac{1}{ip\sqrt{z(1-z)(z-p^{-2})}}$$
$$= \frac{-i}{p}F\left(\arcsin\left(\sqrt{\frac{1-u^2}{1-p^{-2}}}\right),\sqrt{1-p^{-2}}\right). \tag{A8}$$

For negative energies, $E < 0$,

$$k_- = i\sqrt{\sqrt{1+|E|/E_{\max}}-1} = i|k_-|, \tag{A9}$$

$$p = i\sqrt{\frac{E_{\max}}{|E|}}\left(1+\sqrt{1+\frac{|E|}{E_{\max}}}\right) = i|p|, \tag{A10}$$

and therefore we will use the relation

$$K(ik) = \frac{1}{\sqrt{k^2+1}}K\left(\sqrt{\frac{k^2}{k^2+1}}\right) \tag{A11}$$

in Eq. (A4).

In conclusion, the density of states for $E < 0$ and $E > 0$ are, respectively,

$$N(E<0) = \frac{1}{\sqrt{2\alpha'}\pi^2}\int_0^{k_+} dk_x\,\frac{1}{\sqrt{\frac{\alpha}{2}k_x^2 - \frac{\beta}{4}k_x^4 - E}}$$
$$= -i\sqrt{\frac{2}{\beta\alpha'}}\frac{1}{\pi^2 i|k_-|}K(i|p|)$$
$$= -\sqrt{\frac{2}{\beta\alpha'}}\frac{1}{\pi^2|k_-|}\frac{1}{\sqrt{|p|^2+1}}K\left(\sqrt{\frac{1}{1+|p|^{-2}}}\right) \tag{A12}$$

and

$$N(E>0) = \frac{1}{\sqrt{2\alpha'}\pi^2}\int_{k_-}^{k_+} dk_x\,\frac{1}{\sqrt{\frac{\alpha}{2}k_x^2 - \frac{\beta}{4}k_x^4 - E}}$$
$$= -\sqrt{\frac{2}{\beta\alpha'}}\frac{1}{\pi^2 k_+}K(\sqrt{1-p^{-2}}). \tag{A13}$$

The final step is to analyze the asymptotic behavior of the DOS. Since K will show a logarithmical divergence when

$$K(k=1-\eta) \xrightarrow{\eta\to 0} \tfrac{1}{2}\ln|\eta| + O(1), \tag{A14}$$

for $E \to 0$, both the quantities $\sqrt{\frac{1}{1+|p|^{-2}}}$ and $\sqrt{1-p^{-2}}$ approach one. By using $k_\pm \to \sqrt{2}k_{\max}$, $|k_-| \to k_{\max}\sqrt{\frac{|E|}{2E_{\max}}}$, $|p| \to 2\sqrt{\frac{E_{\max}}{|E|}}$, and $\frac{1}{\sqrt{|p|^2+1}} \to \frac{1}{2}\sqrt{\frac{|E|}{E_{\max}}}$, we obtain the DOS at the VHS as

$$N(E\to 0_-) = \frac{1}{2\pi^2}\sqrt{\frac{1}{\alpha\alpha'}}\left[\ln\left(\frac{E_{\max}}{|E|}\right) + O(1)\right] \tag{A15}$$

and similarly,

$$N(E\to 0_+) = \frac{1}{2\pi^2}\sqrt{\frac{1}{\alpha\alpha'}}\left[\ln\left(\frac{E_{\max}}{E}\right) + O(1)\right]. \tag{A16}$$

After multiplication by the unit cell area $a_x \times a_y$, we obtain the result reported in Eq. (4).

APPENDIX B: BARE SPIN SUSCEPTIBILITY AT THE VHS AND THE EFFECT OF DOPING

First, we derive the bare susceptibility when the Fermi energy is at $E_{\mathrm{VHS}} = 0$ ($\mu = 0$). The spin susceptibility is given by

$$\chi(T) = \frac{a_x a_y}{(2\pi)^2}\int d^2k\,\frac{1}{4T}\cosh^{-2}\left(\frac{E_k}{2T}\right)$$
$$= \frac{1}{4T}\int_{-\infty}^{E_{\max}} dE\,N(E)\cosh^{-2}\left(\frac{E}{2T}\right)$$
$$\approx \frac{1}{4T}\int_{-\Lambda}^{\Lambda} dE\,N_0\ln\left(\frac{\bar{\Lambda}}{|E|}\right)\cosh^{-2}\left(\frac{E}{2T}\right)$$
$$= \frac{1}{2}N_0\int_{-\Lambda/2T}^{\Lambda/2T} dx\,\ln\left(\frac{\bar{\Lambda}/2T}{|x|}\right)\cosh^{-2}x$$

$$
\begin{aligned}
&= -N_0 \int_0^{\Lambda/2T} dx \frac{\ln x}{\cosh^2 x}\\
&\quad + N_0 \ln\left(\frac{\bar{\Lambda}}{2T}\right) \int_0^{\Lambda/2T} dx\, \cosh^{-2} x,
\end{aligned}
$$

where we have considered only the contribution from the VHS and the logarithmic behavior applies when $|E| < \Lambda$ and $\bar{\Lambda}$ is another energy cutoff $\bar{\Lambda} < E_{\max}$.

If we then consider the limit $\Lambda \gg T$ and use the formulas

$$
\int_0^{\infty} dx \frac{\ln x}{\cosh^2 x} = \log \frac{\pi}{4} - \gamma_e \equiv -C = -0.8188 \tag{B1}
$$

(γ_e is the Euler-Mascheroni constant) and

$$
\int_0^{\Lambda/2T} dx\, \cosh^{-2} x = \tanh \frac{\Lambda}{2T} \approx 1, \tag{B2}
$$

we obtain the following expression for the bare susceptibility:

$$
\chi(T) \approx N_0 C + N_0 \ln\left(\frac{\bar{\Lambda}}{2T}\right) \equiv N_0 \ln(\omega_D/T), \tag{B3}
$$

which is Eq. (7) in the main text.

Then, we discuss the effect of doping on the susceptibility. When we shift the Fermi energy from zero (E_{VHS}) to μ, the VHS will change to $-\mu$, and therefore we can replace the DOS by $N(E) \approx N_0 \ln \frac{\Lambda}{|E+\mu|}$ for $|E + \mu| < \Lambda$. The susceptibility thus becomes

$$
\begin{aligned}
\chi(T) &\approx \frac{1}{4T} N_0 \int_{-\Lambda-\mu}^{\Lambda-\mu} dE\, \ln\left(\frac{\bar{\Lambda}}{|E+\mu|}\right) \cosh^{-2}\left(\frac{E}{2T}\right)\\
&= \frac{1}{4T} N_0 \int_{-\Lambda}^{\Lambda} dE\, \ln \frac{\bar{\Lambda}}{|E|} \cosh^{-2}\left(\frac{E-\mu}{2T}\right).
\end{aligned} \tag{B4}
$$

We will now consider two regimes: $T \gg \mu$ and $T \ll \mu$. Let us start with the case $T \gg \mu$. By using the expansion

$$
\begin{aligned}
\cosh\left(\frac{E-\mu}{2T}\right) &= \cosh\left(\frac{E}{2T}\right) \cosh\left(\frac{\mu}{2T}\right) +\\
&\quad - \sinh\left(\frac{E}{2T}\right) \sinh\left(\frac{\mu}{2T}\right),
\end{aligned} \tag{B5}
$$

and the approximation

$$
\cosh^{-2}\left(\frac{E-\mu}{2T}\right) \approx \cosh^{-2}\left(\frac{E}{2T}\right) \cosh^{-2}\left(\frac{\mu}{2T}\right), \tag{B6}
$$

the susceptibility can be written as

$$
\begin{aligned}
\chi(T \gg \mu) &\approx \frac{1}{4T} N_0 \int_{-\Lambda}^{\Lambda} dE\, \ln \frac{\bar{\Lambda}}{|E|} \cosh^{-2}\left(\frac{E}{2T}\right)\\
&\quad \times \cosh^{-2}\left(\frac{\mu}{2T}\right) && \text{(B7)}\\
&= N_0 \ln(\omega_D/T) \cosh^{-2}\left(\frac{\mu}{2T}\right)\\
&\approx N_0 \ln(\omega_D/T) && \text{(B8)}
\end{aligned}
$$

and therefore, in this regime, the susceptibility is the same as the undoped case [compare to Eq. (B3)].

On the other hand, when $T \ll \mu$, the function $\cosh^{-2}(\frac{E-\mu}{2T})$ decreases proportionally to $\exp(\frac{\mu-E}{T})$ for $|E-\mu| \gg T$. Therefore it is a good approximation to replace $\ln \frac{\bar{\Lambda}}{|E|} \cosh^{-2}(\frac{E-\mu}{2T})$ by $\ln \frac{\bar{\Lambda}}{|\mu|} \cosh^{-2}(\frac{E-\mu}{2T})$ in the integrand in Eq. (B4). As a result,

$$
\begin{aligned}
\chi(T \ll \mu) &\approx \frac{1}{4T} N_0 \int_{-\Lambda}^{\Lambda} dE\, \ln \frac{\bar{\Lambda}}{|E|} \cosh^{-2}\left(\frac{E-\mu}{2T}\right)\\
&= \frac{1}{4T} N_0 \int_0^{\Lambda} dE\, \ln \frac{\bar{\Lambda}}{|E|} \left[\cosh^{-2}\left(\frac{E-\mu}{2T}\right)\right.\\
&\quad \left. \times \cosh^{-2}\left(\frac{E+\mu}{2T}\right) + \cosh^{-2}\left(\frac{E+\mu}{2T}\right)\right]\\
&\approx \frac{1}{4T} N_0 \int_0^{\Lambda} dE\, \ln \frac{\bar{\Lambda}}{\mu} \left[\cosh^{-2}\left(\frac{E-\mu}{2T}\right)\right.\\
&\quad \left. \times \cosh^{-2}\left(\frac{E+\mu}{2T}\right) + \cosh^{-2}\left(\frac{E+\mu}{2T}\right)\right].
\end{aligned} \tag{B9}
$$

Then, using

$$
\begin{aligned}
&\int_0^{\Lambda} dE\, \cosh^{-2}\left(\frac{E \pm \mu}{2T}\right)\\
&\quad = 2T\left[\tanh\left(\frac{\Lambda \mp \mu}{2T}\right) \pm \tanh\left(\frac{\mu}{2T}\right)\right]
\end{aligned} \tag{B10}
$$

we obtain

$$
\begin{aligned}
\chi(T \ll \mu) &= \frac{1}{2} N_0 \ln \frac{\bar{\Lambda}}{\mu}\left[\tanh\left(\frac{\Lambda+\mu}{2T}\right) + \tanh\left(\frac{\Lambda-\mu}{2T}\right)\right]\\
&= \frac{1}{2} N_0 \ln \frac{\bar{\Lambda}}{\mu} \frac{\sinh \frac{\Lambda}{T}}{\cosh \frac{\Lambda+\mu}{2T} \cosh \frac{\Lambda-\mu}{2T}}\\
&\approx N_0 \ln \frac{\bar{\Lambda}}{\mu} \tanh \frac{\Lambda}{T} \approx N_0 \ln \frac{\bar{\Lambda}}{\mu}.
\end{aligned} \tag{B11}
$$

The final result of Eq. (B11) indicates that, in this regime, the bare spin susceptibility is independent of temperature, as seen in Fig. 3(b). This behavior originates from the infrared cutoff of the excitations due to the thermal distribution. Let us in fact consider the integrand in Eq. (B9):

$$
\begin{aligned}
&\ln \frac{\bar{\Lambda}}{|E|}\left[\cosh^{-2}\left(\frac{E-\mu}{2T}\right) + \cosh^{-2}\left(\frac{E+\mu}{2T}\right)\right]\\
&\quad \simeq \ln \frac{\bar{\Lambda}}{|E|} \cosh^{-2}\left(\frac{E-\mu}{2T}\right).
\end{aligned} \tag{B12}
$$

Due to the chemical potential shift μ, the thermal distribution function $\cosh^{-2}(\frac{E-\mu}{2T}) \sim \exp[-\frac{1}{\sqrt{2}}(\frac{E-\mu}{2T})^2]$ is now centered at $E = \mu$ and not at $E = 0$ like in the undoped case. Therefore, the integration around $E = 0$, where the logarithmic function diverges, now makes essentially no contribution to the total integral, giving rise to the flattening of the susceptibility observed for $T \ll \mu$.

[1] L. Van Hove, Phys. Rev. **89**, 1189 (1953).
[2] M. Fleck, A. M. Oles, and L. Hedin, Phys. Rev. B **56**, 3159 (1997).
[3] R. Hlubina, S. Sorella, and F. Guinea, Phys. Rev. Lett. **78**, 1343 (1997).
[4] H. Q. Lin and J. E. Hirsch, Phys. Rev. B **35**, 3359 (1987).
[5] W. Kohn and J. M. Luttinger, Phys. Lett. **15**, 524 (1965).
[6] J. E. Hirsch and D. J. Scalapino, Phys. Rev. Lett. **56**, 2732 (1986).
[7] C. Honerkamp and M. Salmhofer, Phys. Rev. Lett. **87**, 187004 (2001).
[8] I. M. Lifshitz, Sov. Phys. JETP **11**, 1130 (1960).
[9] Y. Yamaji, T. Misawa, and M. Imada, J. Phys. Soc. Jpn. **75**, 094719 (2006).
[10] N. S. Vidhyadhiraja, A. Macridin, C. Sen, M. Jarrell, and M. Ma, Phys. Rev. Lett. **102**, 206407 (2009).
[11] K.-S. Chen, S. Pathak, S. X. Yang, S. Q. Su, D. Galanakis, K. Mikelsons, M. Jarrell, and J. Moreno, Phys. Rev. B **84**, 245107 (2011).
[12] Y. Okamoto, A. Nishio, and Z. Hiroi, Phys. Rev. B **81**, 121102(R) (2010).
[13] W. Jiang, S. N. Mao, X. X. Xi, Xiuguang Jiang, J. L. Peng, T. Venkatesan, C. J. Lobb, and R. L. Greene, Phys. Rev. Lett. **73**, 1291 (1994).
[14] Y. Dagan, M. M. Qazilbash, C. P. Hill, V. N. Kulkarni, and R. L. Greene, Phys. Rev. Lett. **92**, 167001 (2004).
[15] K.-S. Chen, Z. Y. Meng, T. Pruschke, J. Moreno, and M. Jarrell, Phys. Rev. B **86**, 165136 (2012).
[16] D. M. Newns, C. C. Tsuei, R. P. Huebener, P. J. M. van Bentum, P. C. Pattnaik, and C. C. Chi, Phys. Rev. Lett. **73**, 1695 (1994).
[17] S. D. Obertelli, J. R. Cooper, and J. L. Tallon, Phys. Rev. B **46**, 14928 (1992).
[18] J. L. Cohn, S. A. Wolf, V. Selvamanickam, and K. Salama, Phys. Rev. Lett. **66**, 1098 (1991).
[19] B. Fisher, J. Genossar, C. G. Kuper, L. Patlagan, G. M. Reisner, and A. Knizhnik, Phys. Rev. B **47**, 6054 (1993).
[20] D. M. Newns, H. R. Krishnamurthy, P. C. Pattnaik, C. C. Tsuei, and C. L. Kane, Phys. Rev. Lett. **69**, 1264 (1992).
[21] R. S. Markiewicz, J. Phys. Chem. Solids **58**, 1179 (1997).
[22] H. Liu, A. T. Neal, Z. Zhu, Z. Luo, X. Xu, D. Tomanek, and P. D. Ye, ACS Nano **8**, 4033 (2014).
[23] A. S. Rodin, A. Carvalho, and A. H. Castro Neto, Phys. Rev. Lett. **112**, 176801 (2014).
[24] M. Buscema, D. J. Groenendijk, S. I. Blanter, G. A. Steele, H. S. J. van der Zant, and A. Castellanos-Gomez, Nano Lett. **14**, 3347 (2014).
[25] L. Li, Y. Yu, G. J. Ye, Q. Ge, X. Ou, H. Wu, D. Feng, X. H. Chen, and Y. Zhang, Nat. Nanotechnol. **9**, 372 (2014).
[26] S. P. Koenig, R. A. Doganov, H. Schmidt, A. H. Castro Neto, and B. Ozyilmaz, Appl. Phys. Lett. **104**, 103106 (2014).
[27] R. A. Doganov *et al.*, Nat. Commun. **6**, 6647 (2015).
[28] N. Gillgren *et al.*, 2D Mater. **2**, 011001 (2015).
[29] J. W. Jaing and H. S. Park, Nat. Commun. **5**, 4727 (2014).
[30] P. Giannozzi *et al.*, J. Phys.: Condens. Matter **21**, 395502 (2009).
[31] J. P. Perdew, A. Ruzsinszky, G. I. Csonka, O. A. Vydrov, G. E. Scuseria, L. A. Constantin, X. Zhou, and K. Burke, Phys. Rev. Lett. **100**, 136406 (2008).
[32] P. E. Blochl, Phys. Rev. B **50**, 17953 (1994).
[33] H. J. Monkhorst and J. D. Pack, Phys. Rev. B **13**, 5188 (1976).
[34] N. Marzari and D. Vanderbilt, Phys. Rev. B **56**, 12847 (1997).
[35] N. Marzari, A. A. Mostofi, J. R. Yates, I. Souza, and D. Vanderbilt, Rev. Mod. Phys. **84**, 1419 (2012).
[36] I. Souza, N. Marzari, and D. Vanderbilt, Phys. Rev. B **65**, 035109 (2001).
[37] A. A. Mostofi, J. R. Yates, Y. Lee, I. Souza, D. Vanderbilt, and N. Marzari, Comput. Phys. Commun. **178**, 685 (2008).
[38] J. P. Perdew and Y. Wang, Phys. Rev. B **45**, 13244 (1992).
[39] J. P. Perdew, K. Burke, and M. Ernzerhof, Phys. Rev. Lett. **77**, 3865 (1996).
[40] A. V. Krukau, O. A. Vydrov, A. F. Izmaylov, and G. E. Scuseria, J. Chem. Phys. **125**, 224106 (2006).
[41] M. S. Hybertsen and S. G. Louie, Phys. Rev. B **34**, 5390 (1986).
[42] L. Hedin, Phys. Rev. **139**, A796 (1965).
[43] F. Fuchs, J. Furthmuller, F. Bechstedt, M. Shishkin, and G. Kresse, Phys. Rev. B **76**, 115109 (2007).
[44] B. G. Janesko, T. M. Henderson, and G. E. Scuseria, Phys. Chem. Chem. Phys. **11**, 443 (2009).
[45] N. Troullier and J. L. Martins, Phys. Rev. B **43**, 1993 (1991).
[46] S. Ismail-Beigi, Phys. Rev. B **73**, 233103 (2006).
[47] X. Gonze *et al.*, Comput. Phys. Commun. **180**, 2582 (2009).
[48] J. P. Perdew and M. Levy, Phys. Rev. Lett. **51**, 1884 (1983).
[49] A. N. Rudenko and M. I. Katsnelson, Phys. Rev. B **89**, 201408 (2014).
[50] A. Ziletti, A. Carvalho, P. E. Trevisanutto, D. K. Campbell, D. F. Coker, and A. H. Castro Neto, Phys. Rev. B **91**, 085407 (2015).
[51] V. Tran, R. Soklaski, Y. Liang, and L. Yang, Phys. Rev. B **89**, 235319 (2014).
[52] P. Li and I. Appelbaum, Phys. Rev. B **90**, 115439 (2014).
[53] C. Kittel, *Quantum Theory of Solids*, 2nd revised printing ed. (Wiley, New York, 1987).
[54] T. M. Henderson, J. Paier, and G. E. Scuseria, Phys. Status Solidi B **248**, 767 (2011).
[55] F. Aryasetiawan, Phys. Rev. B **46**, 13051 (1992).
[56] B. Kralik, E. K. Chang, and S. G. Louie, Phys. Rev. B **57**, 7027 (1998).
[57] S. Yanagisawa, Y. Morikawa, and A. Schindlmayr, Jpn. J. Appl. Phys. **53**, 05FY02 (2014).
[58] S. Yanagisawa, Y. Morikawa, and A. Schindlmayr, Phys. Rev. B **88**, 115438 (2013).
[59] G. Grosso and G. Pastori Parravicini, *Solid State Physics* (Academic Press, London, 2000).
[60] J. L. McChesney, A. Bostwick, T. Ohta, T. Seyller, K. Horn, J. Gonzalez, and E. Rotenberg, Phys. Rev. Lett. **104**, 136803 (2010).
[61] A. Abrikosov, J. Campuzano, and K. Gofron, Physica C **214**, 73 (1993).
[62] K. Gofron, J. C. Campuzano, A. A. Abrikosov, M. Lindroos, A. Bansil, H. Ding, D. Koelling, and B. Dabrowski, Phys. Lett. **73**, 3302 (1994).
[63] A. Piriou, N. Jenkins, C. Berthod, I. Maggio-Aprile, and O. Fischer, Nat. Commun. **2**, 221 (2011).
[64] V. Alvarez, J. Gonzalez, F. Guinea, and M. A. H. Vozmediano, J. Phys. Soc. Jpn. **67**, 1868 (1998).
[65] E. C. Stoner, Proc. R. Soc. London, Ser. A **169**, 339 (1939).
[66] J. Bardeen, L. N. Cooper, and J. R. Schrieffer, Phys. Rev. **108**, 1175 (1957).
[67] V. Y. Irkhin, A. A. Katanin, and M. I. Katsnelson, Phys. Rev. B **64**, 165107 (2001).
[68] A. A. Katanin and A. P. Kampf, Phys. Rev. B **68**, 195101 (2003).

[69] A. A. Katanin, H. Yamase, and V. Yu. Irkhin, J. Phys. Soc. Jpn. **80**, 063702 (2011).

[70] Y. Saito and Y. Iwasa, ACS Nano **9**, 3192 (2015).

[71] J. Tersoff and D. R. Hamann, Phys. Rev. B **31**, 805 (1985).

[72] G. Li, A. Luican, J. M. B. Lopes dos Santos, A. H. Castro Neto, A. Reina, J. Kong, and E. Y. Andrei, Nat. Phys. **6**, 109 (2010).

[73] D. S. Dessau *et al.*, Phys. Rev. Lett. **71**, 2781 (1993).

[74] D. M. King, Z.-X. Shen, D. S. Dessau, D. S. Marshall, C. H. Park, W. E. Spicer, J. L. Peng, Z. Y. Li, and R. L. Greene, Phys. Rev. Lett. **73**, 3298 (1994).

[75] W. D. Knight and S. Kobayashi, *Knight Shift*, eMagRes (Wiley, Chichester, 2007).